Journal Pre-proofs

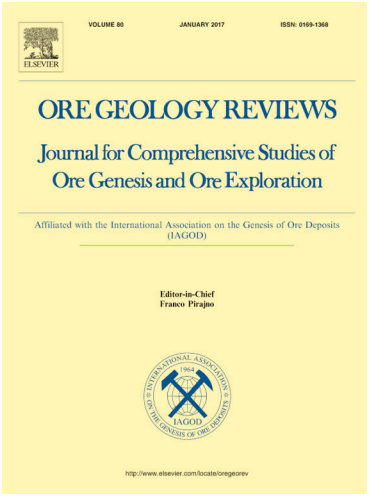

Grain-size characteristics of fine-grained sediments and association with gas hydrate saturation in Shenhu Area, northern South China Sea

Ming Su, Kunwen Luo, Yunxin Fang, Zenggui Kuang, Chengzhi Yang, Jinqiang Liang, Chao Liang, Hui Chen, Zhixuan Lin, Ce Wang, Yaping Lei, Shan Liu, Dorrik A.V. Stow

PII: S0169-1368(20)31074-X
DOI: https://doi.org/10.1016/j.oregeorev.2020.103889
Reference: OREGEO 103889

To appear in: *Ore Geology Reviews*

Received Date: 18 May 2020
Revised Date: 9 November 2020
Accepted Date: 15 November 2020

Please cite this article as: M. Su, K. Luo, Y. Fang, Z. Kuang, C. Yang, J. Liang, C. Liang, H. Chen, Z. Lin, C. Wang, Y. Lei, S. Liu, D.A.V. Stow, Grain-size characteristics of fine-grained sediments and association with gas hydrate saturation in Shenhu Area, northern South China Sea, *Ore Geology Reviews* (2020), doi: https://doi.org/10.1016/j.oregeorev.2020.103889

Grain-size characteristics of fine-grained sediments and association with gas hydrate saturation in Shenhu Area, northern South China Sea

Ming Su[1, 2, 3], Kunwen Luo[1, 2], Yunxin Fang[4], Zenggui Kuang[4], Chengzhi Yang[4], Jinqiang Liang[4], Chao Liang[5], Hui Chen[1, 3] *, Zhixuan Lin[1, 2], Ce Wang[1, 2, 3], Yaping Lei[1, 2, 3], Shan Liu[1, 2, 3], Dorrik A.V. Stow[6]

1. School of Marine Sciences, Sun Yat-sen University, Zhuhai, Guangdong, 519082, China;

2. Guangdong Provincial Key Laboratory of Marine Resources and Coastal Engineering, Guangzhou Guangdong, 510006, China;

3. Southern Marine Science and Engineering Guangdong Laboratory (Zhuhai), Zhuhai Guangdong, 519000, China;

4. Guangzhou Marine Geological Survey, Guangzhou Guangdong, 510075, China;

5. Department of Geology, Northwest University, Xi'an, 710069, China;

6. Institute of Geo-Energy Engineering, Heriot-Watt University, Edinburgh EH14 4AS, Scotland, UK.

* Corresponding author:

Dr. Hui Chen (hovey11162000@gmail.com; chenhui27@mail.sysu.edu.cn)

School of Marine Sciences, Sun Yat-sen University, Zhuhai, Guangdong, 519082, P.R. China

Tel: (+86) 756-3668556

Revised to OGR

Sep. 22nd, 2020

Abstract

Fine-grained gas hydrate (GH) reservoirs are extensively studied worldwide, among which the Shenhu Area (located on the northern slope of the South China Sea) is a world-class GH exploration area. However, the lithology, physical properties, and depositional origins of the *fine-grained* GH reservoirs are not well known. Understanding how sediment grain-size parameters affect the fine-grained GH reservoir quality could provide and important breakthrough for reservoir evaluation. Eight cores, recovered from various expeditions of the Guangzhou Marine Geological Survey, can be combined with 2D/3D seismic data to provide a rare opportunity to systematically investigate the grain-size characteristics of the GH reservoir, as well as the surrounding sediments.

A combination of lithology, grain size characteristics (mean size, sorting, skewness, kurtosis), high-resolution seismic features, and associated bivariate and cluster analysis results support the identification of two distinct intervals of fine-grained sediments that were deposited by different sedimentary processes. There is a relatively higher content of coarser silt in the lower interval than in the upper interval, and their boundary depths are highly consistent with those of the GH-bearing layer and the overlying non-GH-bearing layer. With respect to the unconsolidated GH-bearing sediments from Well G, both the porosity (52%–64%) and sorting coefficient (1.68–2.2) have limited variation, while high GH saturation (>30%) occurs at the top layer. The positive correlation between saturation and the coarsest one-percentile grain size (R=0.55) reveals that an increase in the coarse fraction/particle size favours the development of a larger pore throat diameter and improves the initial permeability and reservoir properties.

The seismic features and cross-plots of the coarsest one-percentile and median values indicate that the lower thin-bedded fine-grained sediments with hydrate may be fine-grained turbidite complexes, including channels/levees/lobes and mass transport deposits. If this is the case, then it may be inferred that turbidite

sediments provide good reservoir physical properties, favourable for GH formation and accumulation. These insights into the relationship between the Quaternary fine-grained turbidites and GH saturation may promote a clearer understanding of the characteristics and development of fine-grained GH reservoirs globally, including in the Shenhu Area of the South China Sea.

Key words: Fine-grained gas hydrate reservoir; Grain-size pattern; Shenhu Area; South China Sea

1. Introduction

Gas hydrate (GH), also known as methane hydrate, is an ice-like crystalline solid in which gas (mostly methane) is trapped within a water cage under high-pressure and low-temperature conditions (Kvenvolden, 1993). Regarded as a potential clean energy source, GH is characterised by its high energy efficiency, environmental friendliness, and excellent potential for energy storage. For example, one volume of GH decomposition releases 150–180 volumes of methane gas (Sloan and Koh, 2008). GH-bearing deposits, such as those in the Gulf of Mexico, the Nankai Trough, the Cascadia subduction zone, the Bay of Bengal, the Ulleung Basin, and the Shenhu Area in the northern South China Sea (SCS), are attracting increased attention from academia and industry (Abegg et al., 2007; Pohlman et al., 2009; Fujii et al., 2015; Li et al., 2018; Yi et al., 2018; Boswell et al., 2019; Collett et al., 2019; Yamamoto et al., 2019; Portnov et al., 2020). Similar to the 'Petroleum System', the concept of the 'Gas Hydrate Petroleum System' (proposed by Collett, 2009) is used to describe the formation of GH in marine and permafrost environments, including GH stability conditions, gas sources, water availability, gas-bearing fluid migration, sedimentary conditions (reservoir rocks, traps, and seals), and timing. Recent scientific ocean drilling programs and hydrate explorations are documenting several types of deep-water sediments that can serve as hydrate hosts, such as turbidites (Torres

et al., 2008; Noguchi et al., 2011; Riedel et al., 2011; Boswell et al., 2012; Su et al., 2016), mass transport deposits (MTDs, containing with debrites) (Tréhu et al., 2003; Riedel et al., 2012), contourites (Paull et al., 1996), and volcanic ash (He et al., 2012; Kars and Kodama, 2015).

Based on laboratory and field analyses, highly saturated GH is more likely to accumulate in coarse-grained sediments (i.e. sandy; mean >63 μm) because the increasing particle size and coarse-grained fraction (sand content) could significantly increase the reservoir quality (Colwell et al., 2004; Heeschen et al., 2016; Ito et al., 2015; Sun et al., 2014; Zhang et al., 2018). Although GH naturally favours sand-dominated sediments for accumulation, especially over the continental permafrost, GH reservoirs hosted by coarse-grained sediments are estimated to account for a small portion of the GH in marine environments (Collett, 2009). Marine GH-bearing sand reservoirs are reported so far in the Nankai Trough (Tsuji et al., 2004, 2009; Kurihaa et al., 2010; Fujii, et al., 2015) and the Alaminos Canyon region (for a small reservoir) of the Gulf of Mexico (Boswell et al., 2009; 2012). However, according to existing reports, most of the GH within marine environments is preserved in fine-grained deep-water sediments (i.e. muddy and silty; mean <63 μm), as observed in the Cascadia subduction zone, the Bay of Bengal, the Ulleung Basin, the northern SCS, and the Hikurangi Margin of New Zealand (Pohlman et al., 2009; Li et al., 2018; Yi et al., 2018; Boswell et al., 2019; Portnov et al., 2020; Kroeger et al., 2019). Very recently, China successfully conducted a second GH exploitation test within fine-grained sediments (Ye et al., 2020). To fully explore the occurrence mechanism of highly saturated GH within fine-grained sediments is of crucial significance; this includes, but is not limited to, the locations of such resources, their volumes, and their favoured host sediment types and associated reservoir physical properties.

According to detailed analyses of geological, geochemical, and geophysical data from the Guangzhou Marine Geological Survey (GMGS) (Zhang et al., 2002; Wang et al., 2003; Guo et al., 2004; Jiang et al.,

2004, 2005; Wang et al., 2005; Yao, 2005), the Shenhu Area, on the northern continental slope of the SCS, is the chosen location for conducting marine GH exploratory drilling in China (Fig. 1a). A series of exploratory drilling expeditions are reported to have been completed by the GMGS in 2007, 2015, 2016, and 2018 (and are referred to as GMGS1, GMGS3, GMGS4, and GMGS5, respectively), as well as two GH production tests (successfully conducted in 2017 and 2020). Unlike the coarse-grained sand-rich reservoirs in the Nankai Trough (Noguchi et al., 2011) and the Gulf of Mexico (Boswell et al., 2012), both the gas hydrate-bearing sediments (GHBS) and overlying non-gas hydrate-bearing sediments (NGHBS) found in the core samples recovered from GMGS1 contribute to the fine-grained clayey silt and silty clay (Chen et al., 2011; Liu et al., 2012). Given their similar mineral and grain size compositions, these two fine-grained sedimentary layers were suggested to have originated from similar sedimentary environments and to have experienced similar depositional processes (Chen et al., 2013). Later studies, based on the pseudo-3D seismic data and C-M patterns (i.e. cross-plots of the coarsest one-percentile and median values obtained via grain-size analysis) from GMGS1 at the site of Well D (Fig. 1b), suggest that possible thin-bedded fine-grained turbidites may be identified as the hydrate-host layer, which most likely have distinct depositional processes from those of the overlying NGHBS in the Shenhu Area (Su et al., 2016; 2019). These GHBS- and NGHBS-associated fine-grained sediments possess representative research significance for a clearer understanding of the occurrence mechanism of highly saturated GH within fine-grained sediments; therefore, a comprehensive analysis of the 2D/3D seismic data and newly obtained core data will be beneficial. Specifically, an exploration of the mechanism of how sediment grain-size parameters affect the (fine-grained) GH reservoir quality could lead to an important breakthrough for reservoir evaluations (e.g., Siddiqui et al., 2016). The effect of grain-size parameters on the physical reservoir properties of GHBS remains unclear, although Ito et al. (2015) preliminarily investigated and suggested that sediment grain-size parameters (i.e. the sand content,

median grain size, skewness, sorting, and kurtosis) have a certain correlation with the GH saturation from the marine GH-bearing sand reservoirs in the Nankai Trough.

In this study, multiple methods are used to analyse the grain-size parameters of the core sediments (Table 1) recovered from the Shenhu Area and to identify the differences between the GHBS and overlying NGHBS. We utilise an integrated dataset based on eight long sediment cores and 2D/3D seismic data (collected during various GH expeditions conducted by the GMGS) to systematically investigate the lithology, grain-size patterns, and depositional origins of the recovered sediments. The specific objectives of this study are to (1) compare and analyse the seismic facies, lithology, and physical properties of the GHBS and NGHBS from the sediment cores recovered from the northern continental slope of the SCS; (2) evaluate the quantitative correlation between grain-size parameters and GH saturation within the GHBS and explain their influencing mechanisms on the quality of fine-grained GH reservoirs; and (3) reveal the possible origins of the GHBS and associated depositional processes. The results will deepen our understanding of the nature of fine-grained GH reservoirs, not only in the Shenhu Area of the northern SCS, but also worldwide.

2. Materials and methods

2.1 Study area geology

Located on the central part of the northern continental slope of the SCS (Fig. 1a), the Pearl River Mouth Basin forms an essential part of the sediment routing system between the Pearl River and the northwest sub-basin (Su et al., 2019). Between the shelf edge and the earl River Mouth Basin, the seafloor topography has an average slope gradient of approximately 2° (Qiao et al., 2015) and features a relatively rough bathymetry because of 17 SSE-oriented slope-confined submarine canyons (Ding et al., 2013; Li et al., 2016; Su et al., 2019) and widespread mass-wasting events (He et al., 2014; Wang et al., 2014; Qiao et al., 2015).

Tectonically, the Shenhu Area belongs to the Baiyun Sag (Fig. 1a), the largest hydrocarbon-rich depression within the Pearl River Mouth Basin. The Baiyun Sag is a compound graben that has accumulated sediments with a thickness of over 12,000 m during its long-term depression since the Palaeocene. From the bottom up, its stratigraphic sequences are ordered as the Shenhu, Wenchang, Enping, Zhuhai, Zhujiang, Hanjiang, Yuehai, and Wanshan Formations (Pang et al., 2007). The tectonic evolution of the area can be divided into two main phases by an unconformity at approximately 32 Ma related to the Nanhai tectonic event (Zhou et al., 2009). The first phase is associated with several rifting events from the Palaeocene to the Early Oligocene, and the second phase is defined as post-rift subsidence from the Late Oligocene to the present. Since the Late Miocene (circa 11.6 Ma), strongly influenced by the Dongsha and Taiwan tectonic movements, the rate of tectonic subsidence has suddenly increased, and a deep-water environment became prevalent (Sun et al., 2012; Ding et al., 2013; Yu et al., 2014).

Our study targets a region of approximately 850 km^2 within the Shenhu Area, which contains newly available 3D seismic data collected by the GMGS (Fig. 1b). Regional analyses show that within the Shenhu Area, regions with water depths of approximately 500 to 2000 m, seafloor temperatures ranging from 2 to 4 °C, and a geothermal gradient of approximately 44 to 67 °C/km are favourable in the formation of GH (Zhang et al., 2018). A previous study demonstrates that the Wenchang and Enping Formations (47.8–33.9 Ma) are the main source rocks for the Baiyun Sag and are characterised by high organic matter content and maturity (Zhu et al., 2009). The thick organic-rich matter of the upper stratigraphic units (i.e. the Yuehai and Wanshan Formations, 10–2.59 Ma) allows them to produce a large amount of biogenetic gas (Su et al., 2018). The gas-bearing fluid migration pathways in the Shenhu Area comprise regional large-scale faults, gas chimneys, small-scale normal faults, and Quaternary detachment faults (Sun et al., 2012; Yang et al., 2015; Su et al., 2017a). The bottom-simulating reflection (BSR) visible in the high-resolution 3D seismic data

roughly corresponds to the stratigraphic boundary of T1 (i.e. ~2.6 Ma as the Quaternary bottom boundary) (Su et al., 2019) (Fig. 2). All these geological conditions indicate that the study area is promising for GH formation and accumulation, which is also confirmed by a series of GH drilling expeditions conducted since 2007.

2.2 Data and methods

The core samples we investigate in this study are from the GMGS from eight hydrate drilling sites in the Shenhu Area. Cores from Wells A, B, C, and D (collected in 2007; GMGS1) along with cores from Wells E and F (collected in 2015; GMGS3) are from inter-canyon areas, while cores from Wells G and H (collected in 2015; GMGS3) are from within slope-confined submarine canyons (Figs. 1b–1c). Detailed information with respect to these eight sampling sites is shown in Table 1.

All eight sites are investigated using newly available high-resolution 3D seismic data collected by the GMGS. The seismic surveys cover an area of approximately 850 km^2 (Fig. 1b) with a bin spacing of 6.25 m × 12.5 m and a vertical range of 0 to 8000 ms of two-way travel-time (TWTT). The seismic data are analysed using GeoFrame software, which is based on seismic reflection features to promote better recognition of the sedimentary facies of the hydrate-host sediments (Fig. 2). Time-depth conversions are already applied for GMGS1 (Wang et al., 2011) and GMGS3 (Qian et al., 2018; Jin et al., 2020; Wang et al., 2020).

Samples are initially treated in pure water for approximately 12 h, and then sodium hexametaphosphate (0.5 mol/L) is added as a dispersant to prevent the fine particles from aggregating. After 12 h, the treated samples are fully disparate through ultrasonic vibration and high-speed centrifugation; they are finally sent to the GMGS for grain-size measurement with a laser granularity analyser (model MS2000, Malvern Panalytical Ltd, UK). The error range of the results is less than 3%, according to duplicate analyses (Chen et

al., 2011). The grain-size parameters are calculated utilizing the logarithmic (original) Folk and Ward (1957) graphical measures as follows:

$$(1)\quad \text{Mean size} = \frac{\varphi_{16} + \varphi_{50} + \varphi_{84}}{3}$$

$$(2)\quad \text{Sorting} = \frac{\varphi_{84} - \varphi_{16}}{4} + \frac{\varphi_{95} - \varphi_{5}}{6.6}$$

$$(3)\quad \text{Skewness} = \frac{\varphi_{84} + \varphi_{16} - 2\varphi_{50}}{2(\varphi_{84} - \varphi_{16})} + \frac{\varphi_{95} + \varphi_{5} - 2\varphi_{50}}{2(\varphi_{95} - \varphi_{5})}$$

$$(4)\quad \text{Kurtosis} = \frac{\varphi_{95} - \varphi_{5}}{2.44(\varphi_{75} - \varphi_{25})}$$

where φ is the phi-scale grain size ($\varphi = -\log_2 D$, D is the grain diameter in μm) plotted on the x-axis, and the subscripts refer to the specific cumulative percentage (y-axis) and where they intercept the cumulative frequency curve (Wentworth, 1929). The sorting coefficient (Eq. 2) is a measure of the standard deviation of a dataset, which represents the spread of the grain-size distribution. Skewness (Eq. 3) is a measure of the asymmetry of a dataset compared with that of a normal distribution. Kurtosis (Eq. 4) measures the extent to which the central part of a grain-size distribution departs from the normal distribution (i.e. whether it is flatter or more peaked than the normal distribution). The recovery rate of drilling sediment cores is relatively low (i.e., around 40% according to Su et al., 2019), and the grain-size measurements of the fine-grained sediments are discontinuously conducted at depth intervals of approximately 0.5 m for as far as possible (Figs. 3 and 4). Therefore, the number of measurement points in each core is different, as shown in Table 1. The results of the grain-size analysis of the fine-grained sediments are shown in Figs. 3–12.

The GH saturation data for the hydrate host layers of the eight sample sites (Table 1) are already compiled by Chen et al. (2011) and Zhang et al. (2020). The GH saturation is estimated from resistivity logs through an analysis utilizing a modified Archie equation for both GMGS1 and GMGS3 (Chen et al., 2011; Zhang et al., 2020), while the precise saturations at Well G are calculated based on elemental capture spectroscopy logging (Kang et al., 2018). The estimated saturation levels from Cl-anomalies in the pore

waters of Well G correspond well with the saturations calculated from logging; however, the depth of the saturation that is derived from Cl-anomalies cannot be compared with that of the sediment sample from Well G. Therefore, the precise saturation at Well G that we use to investigate the relationship between the GH saturation and grain-size parameters in this study are from the results reported by Kang et al. (2018) (Table 2).

3. Results

3.1 Seismic facies, lithological features, and grain-size composition

3.1.1 Seismic facies

The seismic reflection features above the BSR (roughly corresponding to the stratigraphic boundary of T1=2.6 Ma) are easily observed in the newly released high-resolution 3D seismic data. In sections which are drawn from Wells B–D (Fig. 2a) and G–H (Fig. 2b), two seismic units are identified, namely, Unit I (UI) and Unit II (UII).

In its lower layers, UI mainly comprises three seismic facies with distinct features. The first has short (< 0.5 km) high-amplitude reflectors with concave geometries which truncate in the underlying layers at incision depths of approximately 50 ms TWTT (see incisions in Fig. 2). The second has discontinuous to chaotic reflectors, with moderate to low amplitudes or semi-transparent reflections. Its reflector boundaries are fuzzy to unrecognisable, and they mostly occur within or overlie the concave reflectors from the first group. The third has continuous (sub-)parallel reflectors with moderate to high amplitudes. Their lenticular continuities commonly extend over 1 km with two-directional overlap features; however, they are occasionally broken by small-scale incisions (0.1–0.5 km in width within an incision depth of 10 ms TWTT). The inter-canyon areas containing Wells B–D are mainly associated with the first two seismic facies (Figs.

222 1c and 2a), while the intra-canyon areas containing Wells G–H are associated with the third seismic facies
223 (Figs. 1c and 2b). However, low amplitudes and semi-transparent chaotic packages are also sporadically
224 distributed in the latter area.

225 In the upper layers, UII contains layers of undulating sediments demonstrating (sub-)continuous and
226 (sub-)parallel reflectors with moderate to low amplitudes. In the area containing Wells B–D (Fig. 2a), the
227 undulations consist of crests or ridges that are separated by depressions or troughs with asymmetrical
228 wavelengths of approximately 1 km. The troughs are also symmetrical, as their up-slope flanks are steeper
229 than their downslope flanks. The height of the undulations is approximately 40 m above the seafloor. The
230 seismic reflections crossing the troughs are not continuous and are displaced over 150 ms TWTT by listric
231 faults. With respect to the undulations (Fig. 2b), the seismic reflections crossing the troughs are continuous
232 and undulate much more gently than those shown in Fig. 2a, and no obvious faults are observed. The height
233 of the undulations varies within 10 m above the seafloor, with mostly symmetrical wavelengths of
234 approximately 1 km.

235 **3.1.2 Lithological features and grain size composition**

236 The lithology and grain size compositions of the GHBS of the eight cores are shaded in grey in the
237 columns of Figs. 3–5. Fig. 3 shows the cores collected from GMGS1, whereas Fig. 4 shows the cores
238 collected from GMGS3. The lithologies of both the GHBS and NGHBS at the eight sites are dominated by
239 silt, clayey silt, and silty clay, according to results reported by Chen et al. (2011), Liu et al. (2012), Sun et al.
240 (2017), and Li et al. (2018). Throughout these eight cores, the results of the grain size composition analysis
241 indicate that the sand content is less than 15%, the silt content ranges from 50% to 80%, and the mud content
242 ranges from 15% to 45% (Fig. 5); thus, fine-grained (< 63 μm) sediments account for over 95% of the total
243 content. Consistent with previous studies concerning GMGS1 (Chen et al., 2011; Liu et al., 2012), no clear

244 vertical variations in lithology and grain size composition are observed within each site under the present
245 sampling intervals.
246
247 **3.2 Depth profiles of grain-size parameters and C-M patterns**
248 Figs. 3 and 4 show the depth profiles of the grain-size parameters with respect to the mean grain size,
249 the 8–63 μm silt fraction (sortable silt (SS), which refers to the 10–63 μm silt fraction proposed by McCave
250 et al. (1995)), the sorting coefficient, the skewness, and the kurtosis of the eight cores from GMGS1 and
251 GMGS3. All eight core samples demonstrate very similar and narrow mean grain sizes ranging from 6 to 8
252 φ with no significant vertical or spatial variations (Figs. 3 and 4), where subtle differences of the mean (over
253 0.2) between NGHBS and GHBS appear in wells B, E and H (Table 3). Available data for SS values from
254 wells B, D, E and H vary roughly from 30% to 70%, and subtle differences of the mean (over 5%) between
255 NGHBS and GHBS appear in wells D, G and H (Table 3). Nearly all the calculated sorting coefficient values
256 fall within the range of 1.4 to 2.2 (Figs. 3 and 4; Table 3); thus, the fine-grained sediments in the Shenhu
257 Area can be classified as poorly sorted sediments, according to Folk and Ward (1957) and Ito et al. (2015)
258 (i.e. values of <0.71 for well-sorted sediments, 0.71–1.00 for moderately sorted sediments, and >1.00 for
259 poorly sorted sediments). The calculated skewness values for the samples range from 0 to 0.4, a positive
260 skewness according to Folk and Ward (1957), except for the sites of wells C and D that have negative values
261 (Fig. 3c–3d). Subtle differences of the mean (over 0.05) between NGHBS and GHBS appear in wells B, D,
262 E, G and H (Table 3). The grain size of the samples follows a mesokurtic distribution (near-normal grain-
263 size distribution), as most of the kurtosis values range from 0.8 to 1.2 (Figs. 3 and 4). Subtle differences of
264 the mean (over 0.05) between NGHBS and GHBS appear in wells B and E (Table 3).
265 Fig.6 shows the C-M patterns of the eight cores from GMGS1 and GMGS3. All eight cores show a

similar and narrow range of the M value (4–20 μm) between the GHBS and NGHBS; however, they show a certain variation in the C value. Most C values of the GHBS in these cores range from 50 to 120 μm, while these values range from 40 to 600 μm in the GMGS1 cores and 40 to 200 μm in the GMGS3 cores. Most of the points of the GHBS samples gather in a small area and form a trend line parallel to the C=M baseline (Fig. 6b, 6d, and 6e–6h), while there are still a few points that deviate from the trend line. On the other hand, the value points of the NGHBS samples are dispersed in a wider area, and their primary trend line forms mostly across with the C=M baseline at a significant angle (Fig. 6). In summary, the C and M values and their distribution trends reveal a certain difference between the GHBS and NGHBS.

3.3 Bivariate and cluster analysis results of grain-size parameters

3.3.1 Bivariate analysis result

Two typical sites (Wells D and H) are chosen for bivariate grain-size parameter analysis, and bivariate plots are created for the following grain-size parameter pairs: mean size vs. sorting coefficient, mean size vs. skewness, mean size vs. kurtosis, sorting coefficient vs. skewness, sorting coefficient vs. kurtosis, and kurtosis vs. skewness (Figs. 7 and 8). Based on this analysis, the samples at each site are divided into two groups (GHBS and NGHBS) according to the occurrence of GH. At the site of Well D, the first group (GHBS) yields a mean grain size of 6.18 to 6.79 φ (fine silt), sorting coefficient of 1.54 to 1.86 (poorly sorted), skewness of 0.16 to 0.34 (positively to very positively skewed), and kurtosis of 0.91 to 1.06 (mesokurtic). On the other hand, the second group (NGHBS) yields a mean grain size of 6.31 to 6.97 φ (fine silt), sorting coefficient of 1.82 to 2.28 (mostly very poorly sorted), skewness of −0.17 to 0.15 (mostly nearly symmetrical to negative skewness), and kurtosis of 0.83 to 1.05 (platykurtic to mesokurtic; mostly mesokurtic) (Fig. 7). Similarly, the differences between the GHBS and NGHBS at the site of Well H are apparent in the bivariate

plots, with some exceptions related to mean size vs. sorting coefficient and sorting coefficient vs. kurtosis (Figs. 8a and 8e). The fine-grained sediments with hydrate are characterised by a mean grain size of 6.22 to 7.48 φ (fine to very fine silt), sorting coefficient of 1.56 to 2.02 (poorly to very poorly sorted), skewness of 0.20 to 0.41 (positively to very positively skewed), and kurtosis of 0.9 to 1.12 (mostly mesokurtic). The sediments without hydrate show a mean grain size of 6.14 to 7.97 φ (fine to very fine silt), sorting coefficient of 1.36 to 2.14 (mostly poorly sorted), skewness of 0 to 0.19 (near symmetrical to slightly positively skewed), and kurtosis of 0.85 to 1.1 (platykurtic to mesokurtic) (Fig. 8).

3.3.2 Cluster analysis results

At Wells D and E, all grain-size parameters (i.e. mean size, sorting coefficient, skewness, and kurtosis) are employed for an ordered clustering analysis (Fisher Optimal Division), a clustering analysis method in which the samples are clustered without disorganising their sequences by calculating the differences in parameters and rendering the intergroup variation the smallest and the between-group the largest. The cluster analysis results show there are two groups (categories 1 and 2) within the samples; for Wells D and E, the boundaries between the categories occur at approximately 155.45 m and 120.6 m below the seafloor (mbsf), respectively (Fig. 9). These are highly consistent with the GHBS depths at the two sites, which are approximately 155–177 mbsf and 116.5–192.5 mbsf, respectively (Table 1), as indicated by the grey shading in Fig. 9.

3.4 Correlation analysis results between saturation (porosity) and grain-size parameters within GHBS

3.4.1 Saturation and porosity

According to the available data, a correlation analysis between the saturation (porosity) and the grain-size parameters within the GHBS is only reported to have been conducted for Well G. At this site, a very

good (with slight variability) porosity range of 53% to 63% is estimated in the unconsolidated GHBS (Kang et al., 2018; Table 2). The GH saturation is estimated to be highly variable with a range from 0% to 60% of the pore volume (Kang et al., 2018; Table 2). Higher saturation and porosity occur in the upper layer of the GHBS, while lower saturation and porosity occur in the lower layer (Table 2).

3.4.2 Saturation and coarsest one-percentile grain size (C), skewness, kurtosis, sorting coefficient

The saturation and C, skewness, kurtosis, sorting coefficient of Well G are plotted in cross-plots to analyse their correlation (Figs. 10a, 10c–10d and 11a). The C of the GHBS in Well G ranges from 60 to 120 μm (Fig. 10a). The GH saturation and C plotting in a cross-plot reveal a positive correlation between saturation and C with a correlation coefficient of R=0.55. The GHBS layer of this site yields the skewness values of 0.05 to 0.40 (positively to very positively skewed), kurtosis values of 0.85 to 1.10 (platykurtic to mesokurtic; mostly mesokurtic) and sorting coefficient values of 1.68 to 2.2 (poorly sorted) (Figs. 10c–10d an 11a; Table 3). The results of the correlation analysis reveal that the saturation is positively correlated with the sorting coefficient with a correlation coefficient of R=0.68 (Fig. 11a); however, it is negatively correlated with respect to skewness and kurtosis (R=–0.64 and –0.52, respectively) (Fig. 10c–10d).

Four typical samples (two with high GH saturation from the top layer and two with relatively low saturation from the lower layer) are chosen to investigate the correlation between the shape and parameters of the grain-size distribution curve and GH saturation (Fig. 12). Two samples with saturation >53% yield a saddle-shaped grain-size distribution curve with skewness values of 0.09 and 0.13 (slightly positive skewed), and kurtosis values of 0.87 and 0.93 (platykurtic to mesokurtic) (Figs. 12a–12b). Two samples with saturation <12% yield a unimodal-shaped grain-size distribution curve with skewness values of 0.30 and 0.27 (positively skewed), and kurtosis values of 1.06 and 1.10 (mesokurtic) (Figs. 12c–12d).

4. Discussion

4.1 GHBS vs. NGHBS units

As being documented by Chen et al. (2011), Liu et al. (2012), Sun et al. (2017), and Li et al. (2018), the lithologies of the GHBS and NGHBS at the eight sites across the Shenhu Area are dominated by silt, clayey silt, and silty clay sediments (Fig. 5). Considering the similar lithologies and grain size compositions at each site, Chen et al. (2013) suggests that the GHBS and overlying NGHBS are homogeneous sediment units formed under continuous sedimentary processes. However, a comprehensive investigation of seismic reflections, vertical variations in grain-size parameters, as well as bivariate plots of grain-size parameters of the eight cores from GMGS1 and GMGS3, reveals two distinguishable sets of fine-grained sediments corresponding to layers with or without GH (Figs. 2–4 and 6–9). Although the sorting coefficient fail to present significant vertical changes, the SS, mean size, skewness, and kurtosis parameters, as plotted in Figs. 3 and 4, show that there is a higher content of coarser silt in the lower layer of the GHBS than that of the upper layer of the NGHBS (especially with over 5% of differences in the mean SS in wells D, G and H; Table 3). Meanwhile, the cluster analysis results of Wells D and E (Fig. 9) show that the optimal partition boundaries (approximately 155.45 mbsf and 120.6 mbsf, respectively) are the same as those of the boundaries between the sedimentary layers with or without GH (approximately 155 mbsf and 116.5 mbsf for Wells D and E, respectively) (Table 1). Such consistency in the boundary depths yet again indicates that there are most certainly differences in the origins or sedimentary processes (e.g. Donato et al., 2009; Kim et al., 2013; Ordóñeza et al., 2016) between the GHBS and NHGBS.

This indicates that beyond the lithological features, grain size composition, and sorting coefficient, the parameters of the SS, mean grain size, skewness, and kurtosis may carry more information for 1) indicating different sedimentary processes and 2) revealing the mechanism of how sediment grain-size parameters affect

the (fine-grained) GH reservoir quality. A discussion with respect to the influencing mechanism on reservoir quality, as well as possible differences in the sedimentary processes will be elaborated in later subsections of 4.2.1 and 4.3.3, respectively.

4.2 Dominant constraint mechanism for GH saturation

4.2.1 GH-bearing fine grained reservoir

As mentioned above in Section 4.1, the grain-size parameters reveal a higher content of coarse silt in the lower layer of the GHBS than the upper layer of the NGHBS. With respect to the GHBS, both the grain-size parameters and GH saturation (all available data from Well G) present vertical heterogeneity (Figs. 10 and 11; Table 2). High GH saturation (>30%) occurs in the top layer of the GHBS (Table 2). Here, we find a possible correlation between the GH saturation distribution and the grain-size features and associated GH occurrence mechanism within fine-grained reservoirs. Within the hydrate-host layer, the distribution of GH is heterogeneously related to the physical properties of the reservoirs (i.e. porosity and permeability), which are mainly constrained by a range of depositional and diagenetic parameters (Ajdukiewicz and Lander, 2010; Lai et al., 2018; Morad et al., 2010). Porosity is the ratio of the sum volume of all pore spaces in a rock to the rock volume. The interconnected pores in reservoirs not only store hydrocarbons but also allow oil and gas to pass through (i.e. effective porosity) (Abou-Kassem et al., 2006). The permeability refers to the fluid migration ability, and its level is closely related to the porosity, pore geometry, particle grain size, and pore distribution (Ajdukiewicz and Lander, 2010). The porosity, which determines the storage space capacity, and the permeability, which determines whether gas and liquid can efficiently pass through the pore throat directly, determine the physical properties of GH reservoirs.

The GH-host sediments in this study are still in an unconsolidated state, and all available data from Well

G show that the porosity for GHBS is greater than 50% (52% to 64%, Table 2) with rather limited variation. The traditional oil and gas reservoir evaluation system takes 30% as the lower limit of the very high porosity level; thus, limited variation above this threshold has little influence on indicating the storage space conditions. Meanwhile, available permeability data are calculated from the logging results after the methane gas charging and hydrate consolidation (McKinley et al., 2011; Johnson et al., 2011; Dai et al., 2019), failing to truly reflect the initial permeability properties. Thus, depositional parameters, which include grain size, sorting, shape, rigid grain content, and matrix content, are suggested as the primary parameters controlling the reservoir properties (Ajdukiewicz and Lander, 2010).

This study uses existing data from Well G with respect to the GH saturation, C, kurtosis, skewness and sorting. In traditional oil and gas resource evaluations, the porosity of the reservoir is closely related to the sorting degree of the sediment particles (indicated by the sorting coefficient) (McKinley et al., 2011). The porosity of a well to moderately sorted degree (i.e. with a lower sorting coefficient such as <1) should be higher than that of a poorly sorted degree (Beard and Weyl, 1973; Bell et al., 2018). In this study, however, the sorting coefficient of the sediment grain size of the GHBS in Well G ranges from 1.68–2.2 (Table 3), within the poorly sorted interval (Folk and Ward, 1957; Ito et al., 2015). Using the further division into three sub-intervals of poorly (1 to 1.6), very poorly (1.6 to 2.4) and extremely poorly (>2.4) sorted, the sorting degree of the GHBS in Well G is within the very poorly sorted interval (Figs. 11a and 13). We suggest that such limited variation fails to have a decisive effect on where high saturations concentrate. As the GH-host sediments in this study are unconsolidated, and the porosity is very high throughout (over 50% here, Table 2). When the overall oil and gas storage space is very high with limited variation, the ability to allow gas and liquid to pass through (i.e. pore structure which includes pore size and pore throat; Lai et al., 2018) is what should primarily control the reservoir properties.

The pore size and pore throat cannot be directly tested in unconsolidated sediments; fortunately, the alternative proxy parameters of grain shape, rigid grain content, grain size, and matrix content can help in determining the primary parameters controlling the reservoir properties (Ajdukiewicz and Lander, 2010). As discussed in the above paragraph, the sorting (porosity space) plays a minor role. The grain shape we suggest here does not affect the pore structure because the origin and transport distance of the GHBS remain unchanged (Su et al., 2016, 2019, 2020), resulting in the same grain shape in the vertical profile. The role of rigid grain content on pore structure is that it mainly becomes resistant to compaction when buried, but not for this shallow unconsolidated and thin-bedded GHBS. We aim to obtain the grain size and matrix content information through the correlation analysis results between saturation and C. When both sorting and porosity are little changed, as the size of the sediment particles increases, the pore throat diameter becomes larger and the permeability increases (e.g. Beard and Weyl, 1973; Bell et al., 2018). An investigation of the relationship between the GH saturation and C (Fig. 11a) reveals that there is an obvious positive correlation (with a correlation coefficient of R=0.55) between the storage capacity (indicated by saturation) and the pore throat diameter (indicated by the particle grain size, C). The correlation coefficient between the GH saturation and C indicates that the enhancement/increase in the coarse fraction favours the GH storage capacity (Figs. 11a and 13). Within the same interval of sorting and porosity conditions, the addition of a coarse fraction and an increase in particle grain size can lead to a larger pore throat diameter, which favours the initial permeability and reservoir properties (Beard and Weyl, 1973; Bell et al., 2018). Thus, the permeability, affected by the size of the pore throat diameter, plays a key role in the migration of gas-bearing fluids in the reservoir, which predominantly controls the GH saturation distribution in the fine-grained GHBS in this study.

4.2.2 Silty vs. sandy reservoirs

Worldwide, there are not many published data with respect to the grain-size parameters for fine-grained

420 sediments of GH reservoirs. With respect to the collected data, we find that the majority of fine-grained
421 sediments of GH-hosts are silty reservoirs, and similarly, they are very poorly sorted and share limited
422 variation in the sorting coefficient (1.5-2.0, Bahk et al., 2011, 2013). We surmise that the dominant control
423 of permeability on reservoir physical properties can be universal for GH silty reservoirs (Fig. 13).

424 The investigation by Ito et al. (2015) with respect to detailed grain-size parameters within sandy
425 reservoirs is the only available reference of this sort to date. From their study, we find that the GH saturation
426 has a very good correlation with the sand content and (median) grain size (Fig. 10b), which agrees with the
427 indication of the increase in the coarse-grained content, pore throat diameter, and initial permeability.
428 Moreover, the addition of coarser particles is suggested to contribute to the GH saturation variation in the
429 GH-bearing layer, which is consistent with the laboratory finding that highly saturated GH is more likely to
430 accumulate in coarse-grained sediments (Colwell et al., 2004; Sun et al., 2014; Heeschen et al., 2016; Ito et
431 al., 2015; Zhang et al., 2018a).

432 It is worth noting that the saturation shows a negative correlation ($R=-0.26$) with the sorting
433 coefficient from Ito et al. (2015), while the sorting coefficient itself varies from 0.98 to 2.8 (Fig. 11b). As
434 discussed in Section 4.2.1, although basically within the same poorly sorted interval, the sorting degree within
435 this GH sandy reservoir can be further divided into three sub-intervals (Figs. 11b and 13). The generally
436 poorly sorted sediments (i.e. sorting coefficient between 1 to 1.6) can have the highest porosity which best
437 favours the reservoir properties (Figs. 11b and 13). Likewise, the very poorly sorted interval (i.e. sorting
438 coefficient of 1.6 to 2.4) will be relatively better than that of the extremely poorly sorted interval (i.e. sorting
439 coefficient >2.4) (Figs. 11b and 13). If we focus only on the interval with a sorting coefficient from 1.6 to
440 2.4, the trend of relevance will be lost (Fig. 11b). Using the data from Well G in this study, although the
441 saturation seems to have a positive correlation ($R=0.68$) with the sorting coefficient, the sorting coefficient

varies from 1.68 to 2.2 within the same very poorly sorted interval (Fig. 11a). We suggest that this positive correlation could be an illusion, possibly due to the limited number of test data. This may further imply that it is very risky to deviate from the sorting coefficient classification or to hastily apply its correlation with saturation to evaluate the porosity and reservoir properties.

4.3 Potential origins of the GHBS as fine-grained turbidites

4.3.1 Seismic indicators

Based on the pseudo-3D seismic reflections, two seismic units (UI and UII) are identified above the BSR (~2.6 Ma) (Su et al., 2016; 2019) over both the inter- and intra-canyon areas in the study region (Figs. 1c and 2). Utilizing the seismic criteria used to identify architectural elements for various deep-water depositional systems (Stow and Mayall, 2000; Hubbard et al., 2009; Macauley and Hubbard, 2013) and silty-clay lithologies (Figs. 2–5), UI is more likely to be fine-grained turbidites rather than bottom-current-dominated or hemipelagites. The short high-amplitude reflectors with concave geometries most likely represent minor erosional channels or turbidity-flow channels. Discontinuous to chaotic reflectors with moderate to low amplitudes or semi-transparent reflections may represent channel-filling sediments, such as MTDs interbedded with or without turbidites and hemipelagites. The moderate to high amplitude continuous (sub-)parallel reflectors showing an onlap/downlap relationship with underlying layers (e.g. BSR) may represent turbidite lobes. The small-scale incisions and patches of low amplitudes to semi-transparent chaotic packages can be interpreted as small-scale channels over the lobes and MTDs infilling the channels or interlayered with the lobes. UII is described as sediment waves by Wang et al. (2014a), and it shares significant similarities with the undulated sediments offshore of the Dongsha Islands as reported by Li et al. (2016) (especially sediment types A and C) and interpreted as gravity-driven or slope-creep deformations.

Nevertheless, UII fails to present typical seismic reflection features for classic turbidite depositional systems (e.g. complexes of channels/levees/lobes and MTDs) (Fig. 2).

4.3.2 Indicators of C-M patterns

Seismic UI corresponds to the hydrate-bearing layer at six sites. We can attempt to infer the sedimentary processes responsible for the deposition of GHBS by considering the C-M bivariate cross-plots (Fig. 6). C is the particle size corresponding to 1% of the cumulative grain-size distribution curve, representing the maximum hydrodynamic competence of the current involved in its deposition; the M value is the median particle size, representing the average hydrodynamic energy and current carrying capacity (Passega, 1964). Using this fundamental theory and a large number of samples, Passega (1957; 1964) successfully applied this method to differentiate between the sediments deposited in different environments, such as rivers and tractive current deposits, turbidites, quiet water deposits, and beach deposits. This approach is widely accepted and used within academia and industry (Morales et al., 2006; Cagatay et al., 2012; Szczuciński et al., 2012; Dhivert et al., 2015).

In the GMGS1 cores, the trend lines of the C-M patterns of the GHBS samples in each core are parallel to the C=M baseline, while those from the NGHBS samples are oblique relative to the baseline (Fig. 6a–6d). Likewise, in the GMGS3 cores, the trend lines of the GHBS samples are parallel or subparallel to the C=M baseline (Fig. 6e–6f). A few values of the GHBS samples are observed to be outside of the primary ranges of the trend lines, such as those from the sites of Wells G and H (Figs. 6g–6h). These samples are from the top 1 to 2 m of the hydrate-bearing layers. We infer that such deviations might be related to the locations of the samples, which are from thin-bedded transitional zones between the GHBS and NGHBS. However, it is notable that the overall GHBS trend lines of samples from the Shenhu Area are parallel to the C=M baseline, independent of whether the samples are drawn from the inter-canyon (Figs. 1c and 6b–6c) or intra-canyon

(Figs. 1c and 6e–6h) areas. Thus, based on the classifications of Passega (1957; 1964), it is possible that the fine-grained GHBS in the Shenhu Area may be interpreted as turbidites, an interpretation that is consistent with the explanation from the seismic sections in Fig. 2.

4.3.3 Sedimentary process implications

A clear distinction in deep-water sedimentation is not always possible based on seismic/sedimentary characteristics alone and uncertainties should be reserved in any interpretation (Stow and Smillie, 2020). With existing data, we propose that UI is most likely a fine-grained turbidite complex. If this is true, we may obtain further sedimentary process implications as follows.

(1) These turbidites exhibit distinct reflection groups for the two sections shown in Fig. 2, and these groups may be associated with different sedimentary processes in the Shenhu Area. The turbidite channels and infillings in the inter-canyon area (Figs. 1c and 2a) may be fed by or are connected to small-scale channels in the northern Shenhu Area (beyond our study area, but are described by Su et al., 2016; 2019). The turbidite lobes with onlapping geometries and small-scale channels in the intra-canyon area (Fig. 1c and 2b) may represent major basin-fill sediments from axial transportation processes within submarine canyons (Su et al., 2017b; 2020).

(2) Both the skewness and kurtosis from Well G (in the inter-canyon) show a negative correlation with the GH saturation with R values of –0.64 and –0.52, respectively (Fig. 10c–10d). For the middle-lower layer of the GHBS with low saturation, the skewness curve is over-steepened with respect to coarse components but gentle with respect to fine components and the kurtosis is high (Figs. 4c and 12). It represents an environment that lacks the deposition of coarse silty grains where the sediment grains may experience a relatively low-energy sedimentary environment (Visher, 1969; McLaren and Bowles, 1985; McManus, 1988). Such conditions may be matched with distal or overspilling sediments or fringe lobes under final turbidity

processes with low energy (Hansen et al., 2015). In many cases, they may be interbedded with hemipelagites. For the top layer of the GHBS in Well G with high saturation (over 30%), the skewness curve is saddle-shaped (with both coarse and fine grains) and the kurtosis is low (Figs. 4c and 12). These indicate that the increase in coarse silty content is consistent with that of the GH saturation, where sediment grains may experience a relatively high-energy sedimentary environment in continuous periods and the deposition of coarser silty grains would be allowed (e.g., Stow and Smillie, 2020). Such conditions may be matched on the channel terrace or proximal levee where pulses of turbidity processes with continuously higher energy are common (Hansen et al. 2015). Turbidite channel sands, levee-over bank sands, and sheeted sands are known as favourable hydrocarbon reservoirs with heterogeneity facilitating fluid flow (Peakall et al. 2000; Rozman, 2000).

4.3.4 Turbidites as favourable GH-host sediments

In marine environments, GH preferentially accumulates in rapidly deposited deep-water sediments, such as turbidites, MTDs, and contourites, owing to the preservation of sufficient organic material for generating methane (Claypool and Kaplan, 1974) and forming favourable fluid migration conduits (Dillon et al., 1998). GHBS in the Shenhu Area are preferentially interpreted as fine-grained turbidites in both the inter- and intra-canyon areas, according to the combined seismic and grain-size data. In worldwide field explorations, turbidites are widely reported to host GH in marine environments, such as those in the Nankai Trough, Krishna-Godavari Basin of offshore India, Gulf of Mexico, Hikurangi Margin of New Zealand, and Shenhu Area (Noguchi et al., 2011; Riedel et al., 2011; Boswell et al., 2012; Su et al., 2016). GH preserved in MTDs and contourites have been reported in a few regions, such as the Hydrate Ridge, Ulleung Basin, and Blake Ridge (Tréhu et al., 2003; Riedel et al., 2012; Paull et al., 1996).

In theory, seafloor instability triggers soft sediment redeposition as MTDs, and if the redeposition is

fully developed, they ultimately may evolve into turbidity flow (Shan et al., 2019). Compared with MTDs, turbidites are distributed more broadly within marine environments, and this is more likely to control the distribution of GH, as indicated by field exploration findings. Unlike MTDs, in which their thin basal shear zone serves preferentially as a reservoir (Sun et al., 2020), (coarse-grained) turbidites are usually regarded as good reservoirs because of their thick (sandy) beds and good porosity and permeability physical properties (Kneller, 1995; Dutton, 2008; Yoneda et al., 2015). GH that is preserved in contourites is reportedly located in the Blake Ridge drift, according to the Ocean Drilling Program 164 (Paull et al., 1996). Furthermore, according to the Shipboard Scientific Party, fine-grained contourites serve as the GH-host sediments, with GH saturation maxima from approximately 7% and 8.4% at sites 994 and 995, respectively, to approximately 13.6% at site 997. Such relatively low GH saturation, however, may indicate that fine-grained contourites are not the best host sediments for GH. Coarse-grained contourites, on the other hand, may serve as better host sediments for GH accumulation because of their potential as hydrocarbon reservoirs (Yu et al., 2020). Other deep-water sediment facies, such as pelagites, hemipelagites, and authigenic (bio)chemical deposits, are not yet reported in GH field explorations. Taking the results from global field explorations and our findings in the Shenhu Area, we suggest that fine-grained turbidites are the most favourable host sediments for GH accumulation, and such GH deposits will become more exploitable in the near future.

5. Conclusions

(1) A comprehensive analysis of sediment cores from eight GH wells reveals that although their lithology is dominated by fine-grained sediments, two intervals can be further distinguished. There is a higher content of coarse silt in the lower interval than in the upper interval, and their boundary depths are highly consistent with those that are between the GHBS and overlying NGHBS.

552 (2) Under similar sorting and porosity conditions (using available data from Well G), the positive
553 correlation (R=0.55) between saturation and C (the coarsest one-percentile grain size) reveals that the
554 addition of a coarse fraction and an increase in particle grain size can lead to the development of a larger pore
555 throat diameter, which favours the initial permeability and reservoir properties. The permeability (which is
556 affected by the size of the pore throat) plays a key role in the migration of gas-bearing fluids in the reservoir,
557 which primarily controls the GH saturation distribution in the fine-grained GHBS in this study.
558 (3) Taking all existing data into account, we propose that the GHBS are most likely fine-grained turbidite
559 complexes with channels/levees/lobes and MTDs. If this is the case, turbidite as the favourable reservoir also
560 applies to the GH system. The stronger hydrodynamic turbidity flow can transport and deposit sediments
561 with a coarse fraction and larger particle size, thereby providing better reservoir physical properties and
562 making it favourable for GH formation and accumulation.
563

564 **Acknowledgments**

565 We would like to thank the Guangzhou Marine Geological Survey (GMGS) for sharing the data employed
566 in the study. Erwin Suess and one anonymous reviewer are thanked for their thorough reviews and
567 constructive comments. Ya Gao is thanked for her suggestions for the discussion modification. This study
568 was supported by the National Natural Science Foundation of China (Nos. 41830537, 41976067), the Pearl
569 River S&T Nova Program of Guangzhou (No. 201710010198), the Guangdong Special Fund for Economic
570 Development (Marine Economy) (No. GDME-2018D001), and the China Geological Survey Project (No.
571 DD20190217 and No. DD20190230), the China-ASEAN Maritime Cooperation Fund Project
572 (12120100500017001).
573

References

Abegg, F., Bohrmann, G., Freitag, J., Kuhs, W. 2007. Fabric of gas hydrate in sediments from Hydrate Ridge—results from ODP Leg 204 samples. Geo-Marine Letters. 27, 269-277.

Abou-Kassem, J.H., Ali, S.M.F., Islam, M.R. Chapter 2 - Single-Phase Fluid Flow Equations in Multidimensional Domain. In: Abou-Kassem, J.H., Ali, S.M.F., Islam, M.R., editors. Petroleum Reservoir Simulations: Gulf Publishing Company; 2006. p. 7-41.

Ajdukiewicz, J.M., Lander, R.H. 2010. Sandstone reservoir quality prediction: The state of the art. AAPG Bulletin. 94, 1083-1091.

Bahk, J.J., Um, I.K., Holland, M. 2011. Core lithologies and their constraints on gas-hydrate occurrence in the East Sea, offshore Korea: Results from the site UBGH1-9. Marine and Petroleum Geology. 28, 1943-1952.

Bahk, J.J., Kim, D.H., Chun, J.H., Son, B.K., Kim, J.H., Ryu, B.J., Torres, M.E., Riedel, M., Schultheiss, P. 2013. Gas hydrate occurrences and their relation to host sediment properties: Results from Second Ulleung Basin Gas Hydrate Drilling Expedition, East Sea. Marine and Petroleum Geology. 47, 21-29.

Beard, D.C., Weyl, P.K. 1973. Influence of Texture on Porosity and Permeability of Unconsolidated Sand. AAPG Bulletin. 57, 349-369.

Bell, D., Kane, I.A., Ponten, A.S.M., Flint, S.S., Hodgson, D.M., Barrett, B.J. 2018. Spatial variability in depositional reservoir quality of deep-water channel-fill and lobe deposits. Marine and Petroleum Geology. 98, 97-115.

Kneller, B., 1995. Beyond the turbidite paradigm: physical models for deposition of turbidites and their implications for reservoir prediction. Geological Society. 94, 31-49.

595 Boswell, R., Frye, M., Shelander, D., Shedd, W., McConnelle, D.R., Cook, A. 2012. Architecture of gas-
596 hydrate-bearing sands from Walker Ridge 313, Green Canyon 955, and Alaminos Canyon 21:
597 Northern deepwater Gulf of Mexico. Marine and Petroleum Geology. 34, 134-149.
598 Boswell, R., Shelander, D., Lee, M., Latham, T., Collett, T., Guerin, G., Moridis, G., Reagan, M.,
599 Goldberg, D. 2009. Occurrence of gas hydrate in Oligocene Frio sand: Alaminos Canyon Block 818:
600 Northern Gulf of Mexico. Marine and Petroleum Geology. 26, 1499-1512.
601 Boswell, R., Yoneda, J., Waite, W.F. 2019. India National Gas Hydrate Program Expedition 02 summary
602 of scientific results: Evaluation of natural gas-hydrate-bearing pressure cores. Marine and Petroleum
603 Geology. 108, 143-153.
604 Cagatay, M.N., Erel, L., Bellucci, L.G., Polonia, A., Gasperini, L., Eris, K.K., Sancar, U., Biltekin, D.,
605 Ucarkus, G., Ulgen, U.B., Damci, E. 2012. Sedimentary earthquake records in the Izmit Gulf, Sea of
606 Marmara, Turkey. Sedimentary Geology. 282, 347-359.
607 Chen, F., Su, X., Zhou, Y. 2013. Late Miocene-Pleistocene Calcareous Nannofossil Biostratigraphy of
608 Shenhu Gas Hydrate Drilling Area in the South China Sea and Variations in Sedimentation Rates.
609 Earth Science. 38, 1-9.
610 Chen, F., Zhou, Y., Su, X., Liu, G., Lu, H., Wang, J. 2011. Gas hydrate saturation and its relation with
611 grain size of the hydrate-bearing sediments in the Shenhu area of Northern South China Sea. Marine
612 Geology & Quaternary Geology. 31, 95-100.
613 Claypool, G.E., Kaplan, I.R. The Origin and Distribution of Methane in Marine Sediments. In: Kaplan,
614 I.R., editor. Natural Gases in Marine Sediments. Boston, MA: Springer US; 1974. p. 99-139.

615 Collett, T. Gas Hydrate Petroleum Systems in Marine and Arctic Permafrost Environments. 29th Annual
616 Gulf Coast Section of Society for Sedimentary Geology (GCSSEPM Foundation Bob F Perkins
617 Research Conference). Houston (Texas, USA), December, 2009. p. 6-9.
618 Collett, T.S., Boswell, R., Waite, W.F., Kumar, P., Roy, S.K., Chopra, K., Singh, S.K., Yamada, Y.,
619 Tenma, N., Pohlman, J., Zyrianova, M. 2019. India National Gas Hydrate Program Expedition 02
620 Summary of Scientific Results: Gas hydrate systems along the eastern continental margin of India.
621 Marine and Petroleum Geology. 108, 39-142.
622 Colwell, F., Matsumoto, R., Reed, D. 2004. A review of the gas hydrates, geology, and biology of the
623 Nankai Trough. Chemical Geology. 205, 391-404.
624 Dai, S., Kim, J., Xu, Y., Waite, W.F., Jang, J., Yoneda, J., Collett, T.S., Kumar, P. 2019. Permeability
625 anisotropy and relative permeability in sediments from the National Gas Hydrate Program Expedition
626 02, offshore India. Marine and Petroleum Geology. 108, 705-713.
627 Dhivert, E., Grosbois, C., Rodrigues, S., Desmet, M. 2015. Influence of fluvial environments on sediment
628 archiving processes and temporal pollutant dynamics (Upper Loire River, France). Science of the
629 Total Environment. 505, 121-136.
630 Dillon, W.P., Danforth, W.W., Hutchinson, D.R., Drury, R.M., Taylor, M.H., Booth, J.S. 1998. Evidence
631 for faulting related to dissociation of gas hydrate and release of methane off the southeastern United
632 States. Geological Society of London Special Publications. 137, 293-302.
633 Ding, W., Li, J., Li, J., Fang, Y., Tang, Y. 2013. Morphotectonics and evolutionary controls on the Pearl
634 River Canyon system, South China Sea. Marine Geophysical Research. 34, 221-238.
635 Donato, S.V., Reinhardt, E.G., Boyce, J.I., Pilarczyk, J.E., Jupp, B.P. 2009. Particle-size distribution of
636 inferred tsunami deposits in Sur Lagoon, Sultanate of Oman. Marine Geology. 257, 54-64.

637 Dutton, S.P., 2008. Calcite cement in Permian deep-water sandstones, Delaware Basin, west Texas: Origin,
638 distribution, and effect on reservoir properties. AAPG Bulletin. 92, 765-787.
639 Folk, R.L., Ward, W.C. 1957. Brazos River bar [Texas]; a study in the significance of grain size
640 parameters. Journal of Sedimentary Research. 27, 3-26.
641 Fujii, T., Suzuki, K., Takayama, T., Tamaki, M., Komatsu, Y., Konno, Y., Yoneda, J., Yamamoto, K.,
642 Nagao, J. 2015. Geological setting and characterization of a methane hydrate reservoir distributed at
643 the first offshore production test site on the Daini-Atsumi Knoll in the eastern Nankai Trough, Japan.
644 Marine and Petroleum Geology. 66, 310-322.
645 Guo, T.M., Wu, B.H., Zhu, Y.H., Fan, S.S., Chen, G.J. 2004. A review on the gas hydrate research in
646 China. Journal of Petroleum Science and Engineering. 41, 11-20.
647 Hansen, L.A.S., Callow, R.H.T., Kane, I.A., Gamberi, F., Rovere, M., Cronin, B.T., Kneller, B.C. 2015.
648 Genesis and character of thin-bedded turbidites associated with submarine channels. Marine and
649 Petroleum Geology. 67, 852-879.
650 He, J., Liu, X., Yu, Z., Xie, C., Li, Z. 2012. Factors influencing the porosity of gas hydrate bearing
651 sediments. Science China Earth Sciences. 56, 557-567.
652 He, Y., Zhong, G., Wang, L., Kuang, Z. 2014. Characteristics and occurrence of submarine canyon-
653 associated landslides in the middle of the northern continental slope, South China Sea. Marine and
654 Petroleum Geology. 57, 546-560.
655 Heeschen, K.U., Schicks, J.M., Oeltzschner, G. 2016. The promoting effect of natural sand on methane
656 hydrate formation: Grain sizes and mineral composition. Fuel. 181, 139-147.

657 Hubbard, S.M., de Ruig, M.J., Graham, S.A. 2009. Confined channel-levee complex development in an
658 elongate depo-center: Deep-water Tertiary strata of the Austrian Molasse basin. Marine and Petroleum
659 Geology. 26, 85-112.
660 Ito, T., Komatsu, Y., Fujii, T., Suzuki, K., Egawa, K., Nakatsuka, Y., Konno, Y., Yoneda, J., Jin, Y., Kida,
661 M., Nagao, J., Minagawa, H. 2015. Lithological features of hydrate-bearing sediments and their
662 relationship with gas hydrate saturation in the eastern Nankai Trough, Japan. Marine and Petroleum
663 Geology. 66, 368-378.
664 Jiang, S., Yang, J., Ling, H., Yang, T., Daohua, C., Xue, Z., Junfeng, J., Ni, P. 2004. Search for gas hydrate
665 in the south China sea: a geochemical approach. Marine Geology & Quaternary Geology. 24, 103-109.
666 Jiang, S., Yang, T., Xue, Z., Yang, J., Ling, H., Wu, N., Huang, Y., Liu, J., Chen, D. 2005. Chlorine and
667 Sulfate Concentrations in Pore Waters from Marine Sediments in the North Margin of the South China
668 Sea and Their Implications for Gas Hydrate Exploration. Geoscience. 19, 45-54.
669 Jin, J., Wang, X., Guo, Y., Li, J., Li, Y., Zhang, X., Qian, J., Sun, L. 2020. Geological controls on the
670 occurrence of recently formed highly concentrated gas hydrate accumulations in the Shenhu area,
671 South China Sea. Marine and Petroleum Geology. 116, 104294.
672 Johnson, A., Patil, S., Dandekar, A. 2011. Experimental investigation of gas-water relative permeability for
673 gas-hydrate-bearing sediments from the Mount Elbert Gas Hydrate Stratigraphic Test Well, Alaska
674 North Slope. Marine and Petroleum Geology. 28, 419-426.
675 Kang, D., Liang, J., Kuang, Z., Lu, J.A., Guo, Y., Liang, J., Cai, H., Qu, C. 2018. Application of elemental
676 capture spectroscopy logging in hydrate reservoir evaluation in the Shenhu sea area. Natural Gas
677 Industry. 38, 54-60.

678 Kars, M., Kodama, K. 2015. Authigenesis of magnetic minerals in gas hydrate-bearing sediments in the
679 Nankai Trough, offshore Japan. Geochemistry, Geophysics, Geosystems. 16, 947-961.
680 Kim, W., Doh, S.-J., Yu, Y., Lee, Y.I. 2013. Magnetic evaluation of sediment provenance in the northern
681 East China Sea using fuzzy c-means cluster analysis. Marine Geology. 337, 9-19.
682 Kroeger, K.F., Crutchley, G.J., Kellett, R., Barnes, P.M. 2019. A 3-D Model of Gas Generation, Migration,
683 and Gas Hydrate Formation at a Young Convergent Margin (Hikurangi Margin, New Zealand).
684 Geochemistry, Geophysics, Geosystems. 20, 5126-5147.
685 Kurihara, M., Sato, A., Ouchi, H., Narita, H., Ebinuma, T., Suzuki, K., Masuda, Y., Saeki, T., Yamamoto,
686 K., Fujii, T. 2010. Prediction of production test performances in Eastern Nankai trough methane
687 hydrate reservoirs using 3D reservoir model. In Offshore Technology Conference 2010, OTC 2010
688 (pp. 1892-1913). (Proceedings of the Annual Offshore Technology Conference; Vol. 3). Offshore
689 Technology Conference.
690 Kvenvolden, K.A. 1993. Gas hydrates—geological perspective and global change. Reviews of Geophysics.
691 31, 173-187.
692 Lai, J., Wang, G.W., Wang, Z.Y., Chen, J., Pang, X.J., Wang, S.C., Zhou, Z.L., He, Z.B., Qin, Z.Q., Fan,
693 X.Q. 2018. A review on pore structure characterization in tight sandstones. Earth-Science Reviews.
694 177, 436-457.
695 Li, J.F., Ye, J.L., Qin, X.W., Qiu, H.J., Wu, N.Y., Lu, H.L., Xie, W.W., Lu, J.A., Peng, F., Xu, Z.Q., Lu,
696 C., Kuang, Z.G., Wei, J.G., Liang, Q.Y., Lu, H.F., Kou, B.B. 2018. The first offshore natural gas
697 hydrate production test in South China Sea. China Geology. 1, 5-16.

698 Li, X.S., Zhou, Q.J., Su, T.Y., Liu, L.J., Gao, S., Zhou, S.W. 2016. Slope-confined submarine canyons in
699 the Baiyun deep-water area, northern South China Sea: variation in their modern morphology. Marine
700 Geophysical Research. 37, 95-112.
701 Liu, C., Ye, Y., Meng, Q., He, X., Lu, H., Zhang, J., Liu, J., Yang, S. 2012. The Characteristics of Gas
702 Hydrates Recovered from Shenhu Area in the South China Sea. Marine Geology. 307-310, 22-27.
703 Macauley, R.V., Hubbard, S.M. 2013. Slope channel sedimentary processes and stratigraphic stacking,
704 Cretaceous Tres Pasos Formation slope system, Chilean Patagonia. Marine and Petroleum Geology.
705 41, 146-162.
706 McCave, I.N., Manighetti, B., Robinson, S.G. 1995. Sortable silt and fine sediment size/composition
707 slicing: Parameters for palaeocurrent speed and palaeoceanography. Paleoceanography. 10, 593-610.
708 McKinley, J.M., Atkinson, P.M., Lloyd, C.D., Ruffell, A.H., Worden, R.H. 2011. How Porosity and
709 Permeability Vary Spatially with Grain Size, Sorting, Cement Volume, and Mineral Dissolution in
710 Fluvial Triassic Sandstones: The Value of Geostatistics and Local Regression. Journal of Sedimentary
711 Research. 81, 844-858.
712 McLaren, P., Bowles, D. 1985. The effects of sediment transport on grain-size distributions. Journal of
713 Sedimentary Research. 55, 457-470.
714 McManus, J. Grain size determination and interpretation. In: Tucker, M.E., editor. Techniques in
715 sdimentology: Blackwell Scientific Publications; 1988. p. 63-85.
716 Morad, S., Al-Ramadan, K., Ketzer, J.M., De Ros, L.F. 2010. The impact of diagenesis on the
717 heterogeneity of sandstone reservoirs: A review of the role of depositional facies and sequence
718 stratigraphy. AAPG Bulletin. 94, 1267-1309.

719 Morales, J.A., Delgado, I., Gutierrez-Mas, J.M. 2006. Sedimentary characterization of bed types along the
720 Guadiana estuary (SW Europe) before the construction of the Alqueva dam. Estuarine, Coastal and
721 Shelf Science. 70, 117-131.
722 Noguchi, S., Shimoda, N., Takano, O., Oikawa, N., Inamori, T., Saeki, T., Fujii, T. 2011. 3-D internal
723 architecture of methane hydrate-bearing turbidite channels in the eastern Nankai Trough, Japan.
724 Marine and Petroleum Geology. 28, 1817-1828.
725 Ordóñez, C., Ruiz-Barzola, O., Sierra, C. 2016. Sediment particle size distributions apportionment by
726 means of functional cluster analysis (FCA). CATENA. 137, 31-36.
727 Pang, X., Chen, C., Peng, D., Zhu, M., Shu, Y., He, M., Shen, J., Liu, B. 2007. Sequence Stratigraphy of
728 Deep-water Fan System of Pearl River, South China Sea. Earth Science Frontiers. 14, 220-229.
729 Passega, R. 1957. Texture as Characteristic of Clastic Deposition. AAPG Bulletin. 41, 1952-1984.
730 Passega, R. 1964. Grain size representation by CM patterns as a geologic tool. Journal of Sedimentary
731 Research. 34, 830.
732 Paull, C.K., Matsumoto, R., Wallace, P.J., 1996. Proceedings of the Ocean Drilling Program, Vol. 164,
733 Initial Reports, Gas Hydrate Sampling on the Blake Ridge and Carolina Rise. Ocean Drilling Program,
734 College Station, TX, 1996.
735 Peakall, J., McCaffrey, W.D., Kneller, B.C., Stelting, C.E., McHargue, T.R., Schweller, W.J. 2000. A
736 Process Model for the Evolution of Submarine Fan Channels: Implications for Sedimentary
737 Architecture. In: Bouma, A.H., Stone, C.G., editor. Fine-Grained Turbidites Systems. Unite Kingdom:
738 Geological Society Publishing House; 2000. 2000. p. 73-88.

739 Pohlman, J.W., Kaneko, M., Heuer, V.B., Coffin, R.B., Whiticar, M. 2009. Methane sources and
740 production in the northern Cascadia margin gas hydrate system. Earth and Planetary Science Letters.
741 287, 504-512.
742 Portnov, A., Santra, M., Cook, A.E., Sawyer, D.E. 2020. The Jackalope gas hydrate system in the
743 northeastern Gulf of Mexico. Marine and Petroleum Geology. 111, 261-278.
744 Qian, J., Wang, X., Collett, T.S., Guo, Y., Kang, D., Jin, J. 2018. Downhole log evidence for the
745 coexistence of structure II gas hydrate and free gas below the bottom simulating reflector in the South
746 China Sea. Marine and Petroleum Geology. 98, 662-674.
747 Qiao, S., Su, M., Kuang, Z., Yang, R., Liang, J., Wu, N. 2015. Canyon-related undulation structures in the
748 Shenhu area, northern South China Sea. Marine Geophysical Research. 36, 243-252.
749 Riedel, M., Bahk, J.J., Scholz, N.A., Ryu, B.J., Yoo, D.G., Kim, W., Kim, G.Y. 2012. Mass-transport
750 deposits and gas hydrate occurrences in the Ulleung Basin, East Sea – Part 2: Gas hydrate content and
751 fracture-induced anisotropy. Marine and Petroleum Geology. 35, 75-90.
752 Riedel, M., Collett, T.S., Shankar, U. 2011. Documenting channel features associated with gas hydrates in
753 the Krishna–Godavari Basin, offshore India. Marine Geology. 279, 1-11.
754 Rozman, D.J. Characterization of a fine- grained outer submarine fan deposit, Tanqua- Karoo Basin, South
755 Africa. 2000. In: Bouma, A.H., Stone, C.G., editor. Fine-Grained Turbidites Systems. Unite Kingdom:
756 Geological Society Publishing House; 2000. p. 279-290.
757 Shan, X., Shi, X., Qiao, S., Jin, L., Otharán, G.A., Zavala, C., Liu, J., Zhang, Y., Zhang, D., Xu, T., Fu, C.
758 2019. The fluid mud flow deposits represent mud caps of Holocene hybrid event beds from the widest
759 and gentlest shelf. Marine Geology. 415, 105959.

760 Siddiqui, N.A., Rahman, A.H.A., Sum, C.W., Mathew, M.J., Menier, D. 2016. Onshore Sandstone Facies
761 Characteristics and Reservoir Quality of Nyalau Formation, Sarawak, East Malaysia: An Analogue to
762 Subsurface Reservoir Quality Evaluation. Arabian Journal for Science and Engineering. 41, 267-280.
763 Sloan, E.D., Koh, C.A. Clathrate Hydrates of Natural Gases, 3d ed.: New York, CRC Press, Taylor and
764 Francis Group; 2008. 721 p.
765 Stow, D.A.V., Mayall, M. 2000. Deep-water sedimentary systems: New models for the 21st century.
766 Marine and Petroleum Geology. 17, 125-135.
767 Stow, D., Smillie, Z. 2020. Distinguishing between Deep-Water Sediment Facies: Turbidites, Contourites
768 and Hemipelagites. Geosciences. 10.
769 Su, M., Alves, T.M., Li, W., Sha, Z., Hsiung, K.-H., Liang, J., Kuang, Z., Wu, N., Zhang, B., Chiang, C.-S.
770 2019. Reassessing two contrasting Late Miocene-Holocene stratigraphic frameworks for the Pearl
771 River Mouth Basin, northern South China Sea. Marine and Petroleum Geology. 102, 899-913.
772 Su, M., Jiang, H., Wu, N.Y., Sha, Z.B., Liang, J.Q., Kuang, Z.G., Liu, J., Cong, X.R., Yang, R., Wang,
773 Y.F., 2017b. Two different types of fine-grained turbidites associated with gas hydrates in the Shenhu
774 Area, northern continental slope of the South China Sea. In: 9th International Conference on Gas
775 Hydrates. ICGH, Denver, USA, 25-30, June, 2017.
776 Su, M., Lin, Z., Wang, C., Kuang, Z., Liang, J., Chen, H., Liu, S., Zhang, B., Luo, K., Huang, S., Wu, Q.
777 2020. Geomorphologic and infilling characteristics of the slope-confined submarine canyons in the
778 Pearl River Mouth Basin, northern South China Sea. Marine Geology. 424, 106166.
779 Su, M., Sha, Z., Zhang, C., Wang, H., Wu, N., Yang, R., Liang, J., Qiao, S., Cong, X., Liu, J. 2017a. Types,
780 Characteristics and Significances of Migrating Pathways of Gas-bearing Fluids in the Shenhu Area,
781 Northern Continental Slope of the South China Sea. Acta Geologica Sinica. 91, 219-231.

Su, M., Yang, R., Wang, H., Sha, Z., Liang, J., Wu, N., Qiao, S., Cong, X., 2016. Gas hydrates distribution in the Shenhu area, Northern South China sea: Comparisons between the eight drilling sites with gas hydrate petroleum system. Geologica Acta. 14, 79-100.

Su, P., Liang, J., Peng, J., Zhang, W., Xu, J. 2018. Petroleum systems modeling on gas hydrate of the first experimental exploitation region in the Shenhu area, northern South China sea. Journal of Asian Earth Sciences. 168, 57-76.

Sun, J., Zhang, L., Ning, F., Lei, H., Liu, T., Hu, G., Lu, H., Lu, J., Liu, C., Jiang, G., Liang, J., Wu, N. 2017. Production potential and stability of hydrate-bearing sediments at the site GMGS3-W19 in the South China Sea: A preliminary feasibility study. Marine and Petroleum Geology. 86, 447-473.

Sun, Q., Alves, T. 2020. Petrophysics of fine-grained mass-transport deposits: A critical review. Journal of Asian Earth Sciences. 192, 104291.

Sun, S.-C., Liu, C.-L., Ye, Y.-G., Liu, Y.-F. 2014. Phase behavior of methane hydrate in silica sand. The Journal of Chemical Thermodynamics. 69, 118-124.

Sun, Y., Wu, S., Dong, D., Lüdmann, T., Gong, Y. 2012. Gas hydrates associated with gas chimneys in fine-grained sediments of the northern South China Sea. Marine Geology. 311-314, 32-40.

Szczuciński, W., Kokociński, M., Rzeszewski, M., Chagué-Goff, C., Cachão, M., Goto, K., Sugawara, D. 2012. Sediment sources and sedimentation processes of 2011 Tohoku-oki tsunami deposits on the Sendai Plain, Japan — Insights from diatoms, nannoliths and grain size distribution. Sedimentary Geology. 282, 40-56.

Torres, M.E., Tréhu, A.M., Cespedes, N., Kastner, M., Wortmann, U.G., Kim, J.H., Long, P., Malinverno, A., Pohlman, J.W., Riedel, M., Collett, T. 2008. Methane hydrate formation in turbidite sediments of northern Cascadia, IODP Expedition 311. Earth and Planetary Science Letters. 271, 170-180.

804 Tréhu, A., Bohrmann, G., Torres, M.E., Colwell, F.S. Proceedings of the Ocean Drilling Program, Vol.
805 204, Initial Reports, Drilling Gas Hydrates on Hydrate Ridge. Ocean Drilling Program, College
806 Station, TX, 2003.
807 Tsuji, Y., Ishida, H., Nakamizu, M., Matsumoto, R., Shimizu, S. 2004. Overview of the MITI Nankai
808 Trough Wells: A Milestone in the Evaluation of Methane Hydrate Resources. Resource Geology. 54,
809 3-10.
810 Tsuji, Y., Fujii, T., Hayashi, M., Kitamura, R., Nakamizu, M., Ohbi, K., Saeki, T., Yamamoto, K.,
811 Namikawa, T., Inamori, T., Oikawa, N., Shimizu, S., Kawasaki, M., Nagakubo, S., Matsushima, J.,
812 Ochiai, K., Okui, T., Collett, T., Johnson, A., Knapp, C., Boswell, R. Methane-hydrate Occurrence
813 and Distribution in the Eastern Nankai Trough, Japan: Findings of the Tokai-oki to Kumano-nada
814 Methane-hydrate Drilling Program. In: T. Collett; A. Johnson; C. Knapp; R. Boswell (eds): Natural
815 Gas Hydrates—Energy Resource Potential and Associated Geologic Hazards. AAPG. 2009. p. 228-
816 246
817 Visher, G.S. 1969. Grain size distributions and depositional processes. Journal of Sedimentary Research.
818 39, 1074-1106.
819 Wang, H., Zhang, G., Yang, M., Liang, J., Liang, J., Zhong, G. 2003. Structural circumstance of gas
820 hydrate deposition in the continent margin, the south china sea. Marine Geology & Quaternary
821 Geology. 23, 81-86.
822 Wang, L., Wu, S.-G., Li, Q.-P., Wang, D.-W., Fu, S.-Y. 2014. Architecture and development of a multi-
823 stage Baiyun submarine slide complex in the Pearl River Canyon, northern South China Sea. Geo-
824 Marine Letters. 34, 327-343.

825 Wang, X., Liu, B., Jin, J., Lu, J., Zhou, J., Qian, J., Wu, N. 2020. Increasing the accuracy of estimated
826 porosity and saturation for gas hydrate reservoir by integrating geostatistical inversion and lithofacies
827 constraints. Marine and Petroleum Geology. 115, 104298.
828 Wang, X., Wu, S., Guo, X., Xu, N. 2005. Estimation of gas hydrate saturation in the continental slope, the
829 South China Sea. Marine Geology & Quaternary Geology. 25, 89-95.
830 Wang, X., Wu, S., Lee, M., Guo, Y., Yang, S., Liang, J. 2011. Gas hydrate saturation from acoustic
831 impedance and resistivity logs in the Shenhu area, South China Sea. Marine and Petroleum Geology.
832 28, 1625-1633.
833 Wentworth, C.K. 1929. Method of Computing Mechanical Composition Types in Sediments. Geological
834 Society of America Bulletin. 40, 771-790.
835 Yamamoto, K., Wang, X.X., Tamaki, M., Suzuki, K. 2019. The second offshore production of methane
836 hydrate in the Nankai Trough and gas production behavior from a heterogeneous methane hydrate
837 reservoir. RSC Advances. 9, 25987-26013.
838 Yang, R., Su, M., Qiao, S., Cong, X., Su, Z., Liang, J., Wu, N. 2015. Migration of methane associated with
839 gas hydrates of the Shenhu Area, northern slope of South China Sea. Marine Geophysical Research.
840 36, 253-261.
841 Yao, B. 2005. The forming condition and distribution characteristics of the gas hydrate in the South China
842 Sea. Marine Geology & Quaternary Geology. 25, 81-90.
843 Ye, J.L., Qin, X.W., Xie, W.W., Lu, H.L., Ma, B.J., Qiu, H.J., Liang, J.Q., Lu, J.A., Kuang, Z.G., Lu, C.,
844 Liang, Q.Y., Wei, S.P., Yu, Y.J., Liu, C.S., Li, B., Shen, K.X., Shi, H.X., Lu, Q.P., Li, J., Kou, B.B.,
845 Song, G., Li, B., Zhang, H.E., Lu, H.F., Ma, C., Dong, Y.F., Bian, H. 2020. The second natural gas
846 hydrate production test in the South China Sea. China Geology. 3, 197-209.

Yi, B.Y., Lee, G.H., Kang, N.K., Yoo, D.G., Lee, J.Y. 2018. Deterministic estimation of gas-hydrate resource volume in a small area of the Ulleung Basin, East Sea (Japan Sea) from rock physics modeling and pre-stack inversion. Marine and Petroleum Geology. 92, 597-608.

Yoneda, J., Masui, A., Konno, Y., Jin, Y., Egawa, K., Kida, M., Ito, T., Nagao, J., Tenma, N., 2015. Mechanical properties of hydrate-bearing turbidite reservoir in the first gas production test site of the Eastern Nankai Trough. Marine and Petroleum Geology. 66, 471-486.

Yu, X., Stow, D., Smillie, Z., Esentia, I., Brackenridge, R., Xie, X., Bankole, S., Ducassou, E., Llave, E. 2020. Contourite porosity, grain size and reservoir characteristics. Marine and Petroleum Geology. 117, 104392.

Yu, X., Wang, J., Liang, J., Li, S., Zeng, X., Li, W. 2014. Depositional characteristics and accumulation model of gas hydrates in northern South China Sea. Marine and Petroleum Geology. 56, 74-86.

Zhang, B., Zhou, L., Liu, C., Zhang, Q., Wu, Q., Wu, Q., Liu, C. 2018a. Influence of sediment media with different particle sizes on the nucleation of gas hydrate. Natural Gas Industry. 38, 148-155.

Zhang, G., Huang, Y., Zhu, Y., Wu, B. 2002. Prospect of gas hydrate resources in the south china sea. Marine Geology & Quaternary Geology. 22, 75-81.

Zhang, W., Liang, J., Su, P., Wei, J., Sha, Z., Lin, L., Liang, J., Huang, W. 2018b. Migrating pathways of hydrocarbons and their controlling effects associated with high saturation gas hydrate in Shenhu area, northern South China Sea. Geology of China. 45, 1-14.

Zhang, W., Liang, J., Wei, J., Lu, J., Su, P., Lin, L., Huang, W., Guo, Y., Deng, W., Yang, X., Wan, Z. 2020. Geological and geophysical features of and controls on occurrence and accumulation of gas hydrates in the first offshore gas-hydrate production test region in the Shenhu area, Northern South China Sea. Marine and Petroleum Geology. 114, 104191.

869 Zhou, D., Sun, Z., Liao, J., Zhao, Z., He, M., Wu, X., Pang, X. 2009. Filling history and post-breakup
870 acceleration of sedimentation in Baiyun Sag, deepwater northern South China Sea. Journal of Earth
871 Science. 20, 160.
872 Zhu, W., Huang, B., Mi, L., Wilkins, R., Fu, N., Xiao, X. 2009. Geochemistry, origin and deep-water
873 exploration potential of natural gases in the Pearl River Mouth and Qiongdongnan Basins, South
874 China Sea. AAPG Bulletin. 93, 741-761.

875 # Figure and table captions

876

877 Figure 1. Topographic map showing the location of gas hydrate drilled sites in the Shenhu Area (a) as well
878 as the location of seismic sections used in this study (b). (c): The geomorphic (inter-canyon and intra-canyon
879 areas) evolution of T1 (the base of Quaternary, bottom simulating reflection roughly distributed along this
880 interface, ~2.6 Ma) to T0 (present-day). The capital letters A, B, C, D, E, F, G, and H in the inset figure (c)
881 refer to the gas hydrate drilled sites Well A, B, C, D, E, F, G, and H, respectively.

882

883 Figure 2. (a) and (b): Seismic profile and sketch drawing across Well B-D, and Well G-H, respectively. Two
884 seismic reflection unit are distinguished in both inter-canyon area (a) and intra-canyon area (b); Unit I (gas
885 hydrate-bearing) are preferentially interpreted as fine-grained turbidite complex with channel/levee/lobe and
886 MTD, Unit II were interpreted as sediment waves or seafloor failure deformations (Wang et al., 2014a; Li et
887 al., 2016). BSR (bottom simulating reflection, refer to the base of gas hydrate-bearing sediment) are
888 recognized in both profiles and marked as green dash lines, matching with T1 (~2.6 Ma) as the base of
889 Quaternary.

890

891 Figure 3. Depth profile of sediment grain size distribution parameters and lithology in GMGS1 samples. The
892 lithology of these sediment composed by silt (show as orange in lithology column) and clayey silt (show as
893 yellow in lithology column). The parameters show in these figures include mean size in φ ($\varphi = -\log_2 D$,
894 D is grain diameter in mm), 8-63 μm fraction (sortable silt SS, refer to MaCave et al., 1995), sorting
895 coefficient, skewness, and kurtosis. The gas hydrate-bearing interval are shown as gray shade, samples in
896 these intervals are highlighting as red dots. (a), (b), (c), and (d) refer to Well A, B, C and D, respectively.

897

898 Figure 4. Depth profile of sediment grain size distribution parameters and lithology in GMGS3 samples. The
899 lithology of these sediment composed by silt (show as orange in lithology column) and clayey silt (show as
900 yellow in lithology column). The parameters show in these figures include mean size in φ (φ = - $\log_2$ D,
901 D is grain diameter in mm), 8-63 μm fraction (sortable silt SS, refer to MaCave et al., 1995), sorting
902 coefficient, skewness, and kurtosis. The gas hydrate-bearing interval are shown as gray shade, samples in
903 these intervals are highlighting as red dots. (a), (b), (c), and (d) refer to Well E, F, G and H, respectively.

904

905 Figure 5. Grain size compositional fractions (the average component measured) for sediment samples in the
906 non-gas hydrate-bearing interval and the gas hydrate-bearing interval from wells A to H.

907

908 Figure 6. C-M patterns (the coarsest one percentile grain-size and median grain-size values from grain-size
909 analyses) for GMGS1&3 sites. C and M values are draw in the cross plots. The distribution trend lines of the
910 gas hydrate-bearing sediment (GHBS) samples are marked as red solid lines, and for the gas hydrate-free
911 sediment samples are marked as blue dash lines. The value points of GHBS samples run parallel to the C=M
912 baseline, except few abnormal points; The value points of gas hydrate-free sediment samples run intersecting
913 with the C=M baseline. (a), (b), (c), (d), (e), (f), (g), and (h) refer to Well A, B, C, D, E, F, G and H,
914 respectively.

915

916

917 Figure 7. Sediment grain-size parameter bivariate plots for **Well D**. Gas hydrate-bearing sediment samples
918 are marked as Red pentacle, and gas hydrate-free sediment samples marked as green circle. (a): sorting

coefficient vs. mean size; (b): skewness vs. mean size; (c): kurtosis vs. mean size; (d): skewness vs. sorting coefficient; (e): kurtosis vs. sorting coefficient; (f): kurtosis vs. skewness.

Figure 8. Sediment grain-size parameter bivariate plots for **Well H** drilling site. Gas hydrate-bearing sediment samples are marked as Red pentacle, and gas hydrate-free sediment samples marked as green circle. (a): sorting coefficient vs. mean size; (b): skewness vs. mean size; (c): kurtosis vs. mean size; (d): skewness vs. sorting coefficient; (e): kurtosis vs. sorting coefficient; (f): kurtosis vs. skewness. The figures show that these value points divided into two set respond to gas hydrate-bearing or not, except (a) and (e).

Figure 9. The ordered clustering (Fisher Optimal Division) analysis results of four grain-size parameters (mean size, sorting coefficient, skewness, and kurtosis) for Well D (the left one) and Well E (the right one) sediment cores. The results yield an optimal partition boundary of 155.45 mbsf in Well D, and of 120.6 mbsf in Well E, respectively. Gas hydrate-bearing interval in these two Well are marked as gray shadow.

Figure 10. Relationship between grain-size parameters and gas hydrate saturation for the gas hydrate-bearing sediments from Well G. (a): The coarsest one percentile grain-size (C) vs. gas hydrate saturation; (b): median grain-size vs. gas hydrate saturation (after Ito et al., 2015); (c): skewness vs. gas hydrate saturation; (d): kurtosis vs. gas hydrate saturation. The C and median grain-size (after Ito et al., 2015) are positive correlated with gas hydrate saturation with correlation coefficient R 0.55, 0.72, respectively. Kurtosis and skewness are negative with saturation with correlation coefficient R -0.52, -0.55, respectively.

Figure 11. Relationship between the sorting coefficient and gas hydrate saturation for the gas hydrate-bearing

sediments from (a) Well G in this studyand from (b) the Nankai trough, published by Ito et al., 2015.

Figure 12. Grain-size distribution curves of the representative samples corresponding to high (a and b) and low (c and d) gas hydrate saturation from the gay hydrate-bearing sediments of Well G. (a) and (b): The curves show saddle shapes. (c) and (d): The curves show single asymmetric peak shapes. Sh=Sorting coefficient, Sk=skewness, Ku=Kurtosis, Sh=Gas hydrate saturation.

Figure 13. Model for how difference grain-size parameters effect GH saturation in silty and sandy GH reservoirs

Table 1. Core sample information from eight Guangzhou Marine Geological Survey gas hydrate drilling sites in the Shenhu Area.

Table 2. Gas hydrate saturation and sediment porosity data for Well G, obtained from Kang et al.,2018. For comparable with cored sediment grain-size parameters, we read these data according to the depth of sediment samples.

Table 3. Value comparison of grain-size parameters between the gas hydrate-bearing sediments and non-gas hydrate-bearing sediments from wells B, D, E, F, G, H.

Declaration of interests

☒ The authors declare that they have no known competing financial interests or personal relationships that could have appeared to influence the work reported in this paper.

☐The authors declare the following financial interests/personal relationships which may be considered as potential competing interests:

Table 1. Core sample information from eight Guangzhou Marine Geological Survey gas hydrate drilling sites in the Shenhu Area.

Drilling sites	Sampling depth (mbsf)	GH-bearing layer (mbsf)	Number of samples	GH saturation (ave)	GH saturation (max)
GMGS1					
Well A	0–261.86	–	210	–	–
Well B	20–238.2	191–225	48	25%	47%
Well C	0–175.17	–	164	–	–
Well D	0–194.18	155–177	126	–	44%
GMGS3					
Well E	12–211	116.5–192.5	136	34%	53%
Well F	50–267	209–265	157	33%	76%
Well G	50–174	147–172	71	25%	63%
Well H	52–168	138.3–157.6	106	45%	71%

977 Note: GH: gas hydrate; GMGS: Guangzhou Marine Geological Survey; GMGS1 data edited by Chen et al.,

978 2011 and GMGS3 edited by Zhang et al., 2020.

979

980

Table 2. Gas hydrate saturation and sediemnt porosity data for Well G, obtained from Kang et al.,2018. For ccomparable with cored sediment grain-size parameters, we read these data according to the depth of sediment samples.

Depth(mbsf)	GH saturation(%)	porosity(%)
147.1	55.848	62.922
147.6	54.184	61.013
148.1	46.791	61.364
148.6	48.627	60.571
149.1	55.194	61.195
149.6	54.728	62.946
150.1	44.853	61.477
150.6	40.306	60.36
151.1	28.81	61.152
151.77	44.711	60.915
160.34	36.251	55.582
162.6	13.073	54.931
163.1	24.788	56.896
164.71	17.34	56.471
165.11	5.354	55.453
165.6	23.484	53.72
166.1	9.537	55.04
166.6	17.623	57.916
167.1	32.076	58.267
168.14	15.185	56.796
168.6	18.302	56.062
169.1	10.503	56.762
169.6	4.686	55.384
170.1	4.484	55.726
171.1	19.76	56.173
171.35	16.373	56.554

981

982

Table 3. Value comparison of grain-size parameters between the gas hydrate-bearing sediments and non-gas hydrate-bearin

	Well No.		Sorting coefficient	distinguishable	Mean grain size φ	distinguishable	sortable silt (SS) %	distinguishable	Skewness	dis sha
GMGS1	B	NGHBS	1.53-1.66	×	6.24-7.09 (6.58)	√	29.76-70.5 (53.06)	×	0.21-0.38 (0.25)	
		GHBS	1.61-1.74		6.60-7.31 (6.97)		45.09-61.84 (54.86)		0.12-0.22 (0.17)	
	D	NGHBS	1.71-2.45	×	6.05-6.97 6.59)	×	31-57-63.34 (44.59)	√	`-0.17-0.15 (0.01)	
		GHBS	1.54-2.03		6.13-6.79 (6.41)		60.41-70.55 (64.63)		0.16-0.34 (0.26)	
GMGS3	E	NGHBS	1.16-1.88	×	6.12-7.71 (6.5)	√	no data availiable		0-0.43 (0.26)	
		GHBS	1.42-2.16		6.62-7.91 (7.21)				`-0.02-0.35 (0.19)	
	F	NGHBS	1.48-2.78	×	6.17-7.71 (7.10)	×	no data availiable		0.02-0.36 (0.21)	
		GHBS	1.43-1.8		6.91-7.88 (7.30)				0-0.28 (0.17)	
	G	NGHBS	1.54-2.37	×	5.82-7.58 (6.84)	×	39.54-58.77 (48.71)	√	0-0.24 (0.1)	
		GHBS	1.68-2.2		6.31-7.2 (6.74)		41.29-67.32 (56.69)		0.06-0.38 (0.25)	
	H	NGHBS	1.36-2.14	×	6.14-7.97 (7.23)	√	29.12-61.29 (43.83)	√	0-0.39 (0.10)	
		GHBS	1.56-2.02		6.22-7.63 (6.84)		36.33-69.93 (57.92)		0-0.41 (0.26)	
			>1; poorly sorted		value range (mean)		value range (mean)		value range (mean)	

Highlights

- Distinct grain size characteristics of fine-grained gas/non-gas hydrate-bearing sediments are documented
- Correlation between grain-size parameters and gas hydrate saturation is presented
- Increased coarse fraction/particle size favours reservoir property by improving initial permeability
- Seismic and C-M patterns indicate fine-grained turbidites as potential favored host for gas hydrate